APPLIED SCIENCES AND ENGINEERING

Real-time tracking of fluorescent magnetic spore–based microrobots for remote detection of *C. diff* toxins

Yabin Zhang[1,2], Lin Zhang[3], Lidong Yang[1], Chi Ian Vong[1], Kai Fung Chan[2,4], William K. K. Wu[3,5], Thomas N. Y. Kwong[6,7], Norman W. S. Lo[8], Margaret Ip[8], Sunny H. Wong[5,8,6,7], Joseph J. Y. Sung[6,7], Philip W. Y. Chiu[7,4,9,10], Li Zhang[1,4,10]*

A rapid, direct, and low-cost method for detecting bacterial toxins associated with common gastrointestinal diseases remains a great challenge despite numerous studies and clinical assays. Motion-based detection through tracking the emerging micro- and nanorobots has shown great potential in chemo- and biosensing due to accelerated "chemistry on the move". Here, we described the use of fluorescent magnetic spore–based microrobots (FMSMs) as a highly efficient mobile sensing platform for the detection of toxins secreted by *Clostridium difficile* (*C. diff*) that were present in patients' stool. These microrobots were synthesized rapidly and inexpensively by the direct deposition of magnetic nanoparticles and the subsequent encapsulation of sensing probes on the porous natural spores. Because of the cooperation effect of natural spore, magnetic Fe_3O_4 nanoparticles, and functionalized carbon nanodots, selective fluorescence detection of the prepared FMSMs is demonstrated in *C. diff* bacterial supernatant and even in actual clinical stool samples from infectious patients within tens of minutes, suggesting rapid response and good selectivity and sensitivity of FMSMs toward *C. diff* toxins.

INTRODUCTION

Clostridium difficile (*C. diff*) is a gram-positive anaerobe and gastrointestinal pathogen responsible for hundreds of thousands of nosocomial infections in developed countries (*1*). Infection with these bacteria can trigger a series of *C. diff*–associated diseases, from mild diarrhea to even fatal pseudomembranous colitis (*2*). The as-proven pathogenicity of *C. diff* mainly originates in two high–molecular weight secreted exotoxins, toxin A and toxin B, which result in mucosal damage (*3*). Accurate and timely diagnosis of these toxins is necessary both for early diagnosis of bacterial infection and for the timely implementation of infection control and pharmacological treatments. At present, a series of early diagnostic strategies targeting one or both toxins through conjugation technique have been developed, including enzyme immunoassays, cell culture cytotoxicity neutralization assay, glutamate dehydrogenase assay, and molecular assays (*4*, *5*). However, these assays are limited by high analytical cost, strong dependence on reference, long turnaround time, and widely varying sensitivity and specificity in the diagnostic laboratory setting. The development of a simple, rapid, and real-time monitoring diagnostic approach is imperative and would be helpful to the clinician for the selection of an efficient treatment strategy at the beginning of the infection.

Artificial micro/nanomachines (also called micro/nanorobots), powered in the solution by various types of energy sources, have attracted interest as a relatively new research branch because of the mechanical motion distinctive from conventional micro/nanomaterials (*6*, *7*). This motion feature, together with the easy functionalization inherited from micro/nanomaterials, provides these micro/nanomachines with great potential for the development of a novel remote sensing platform. This mobile sensing platform not only offers real-time and on-site measurement but also causes an "on-the-fly" reaction to accelerate the reaction rate produced by the built-in solution mixing and the improved contact with the continuous rotation-and-translation movement (*8*). Moreover, the tiny sizes of micro- and nanomachines also enable their operation in small and narrow regions. Now, a large number of micro/nanomachines are prepared for various motion-based remote sensing applications (*9*–*12*). Wang and colleagues (*9*) reported an aptamer-based reduced graphene oxide/platinum micromotor for real-time fluorescence detection of the ricin B toxin. Escarpa and colleagues (*10*–*12*) prepared a series of carbon-based catalytic micromotors to detect bacterial endotoxins or analyze mycotoxins in food samples. Most of these micromachines generally show a tubular and Janus morphology and are produced using template-assisted strategies. Moreover, their propulsions commonly rely on chemical fuels, especially hydrogen peroxide (H_2O_2) and surfactants, with the guidance and assistance of external magnetic field (*13*). The strong oxidation of H_2O_2, however, makes a variety of biomolecules denatured and/or changes the detection environments, such as the change of pH value and the introduction of exogenous ions. Moreover, the gradual consumption of H_2O_2 by biomolecules lowers effective motion of micro/nanomachines, finally influencing the detection efficiency. These side effects make the H_2O_2-driven micro/nanomachines not applicable for biosensing in complex physiological environments (*7*, *14*–*16*). In addition, H_2O_2-enriched media with high concentrations (i.e., >1 volume %) are not beneficial for intracellular detection or further biological sensing due to poor biocompatibility (protein denaturation). Moreover, the concentration of H_2O_2 greatly limits the locomotion of micro/nanomachines and makes the sensing process

[1]Department of Mechanical and Automation Engineering, Faculty of Engineering, The Chinese University of Hong Kong, Shatin NT, Hong Kong SAR, China. [2]Department of Biomedical Engineering, Faculty of Engineering, The Chinese University of Hong Kong, Shatin NT, Hong Kong SAR, China. [3]Department of Anaesthesia and Intensive Care, The Chinese University of Hong Kong, Shatin NT, Hong Kong SAR, China. [4]Chow Yuk Ho Technology Centre for Innovative Medicine, The Chinese University of Hong Kong, Shatin NT, Hong Kong SAR, China. [5]Li Ka Shing Institute of Health Science, Faculty of Medicine, The Chinese University of Hong Kong, Shatin NT, Hong Kong SAR, China. [6]Department of Medicine and Therapeutics, Faculty of Medicine, The Chinese University of Hong Kong, Shatin NT, Hong Kong SAR, China. [7]Institute of Digestive Disease, Faculty of Medicine, The Chinese University of Hong Kong, Shatin NT, Hong Kong SAR, China. [8]Department of Microbiology, Faculty of Medicine, The Chinese University of Hong Kong, Shatin NT, Hong Kong SAR, China. [9]Department of Surgery, The Chinese University of Hong Kong, Shatin NT, Hong Kong SAR, China. [10]CUHK T Stone Robotics Institute, The Chinese University of Hong Kong, Shatin NT, Hong Kong SAR, China.
*Corresponding author. Email: lizhang@mae.cuhk.edu.hk

uncontrollable. Besides, mass production is still a challenge for micro/nanoscale structures and the derived artificial sensing micro/nanomachines because they generally require tedious procedures and/or advanced instruments. Exploring the novel scalable methods is thus indispensable to promote the widespread and extensive application of micro/nanomachines in the future.

Spores, which are produced by a wide range of plant or fungi species, commonly exist in nature. A unique and intricate three-dimensional (3D) architecture not only protects the sensitive genetic material from extreme environmental conditions but also enables easy spreading and diffusion by wind or other medium (*17*). These microarchitectures can be renewably produced with highly efficient and reproducible processes. These fascinating features, together with the intrinsic biocompatibility of biological materials, make natural 3D architectures attractive as biotemplates for developing novel functional materials for biomedical applications (*18*, *19*). Combining the bioinspired materials with micro/nanorobots will better use and extend the intrinsic functions of biological materials, e.g., diverse morphology and structure, biocompatibility, and large-scale synthesis (*20*, *21*). The spores used here are obtained from *Ganoderma lucidum* (*G. lucidum*) spores from a kind of fungi named "lingzhi" in China, which have an abundant supply and can be artificially cultured by renewable means. The peculiar morphology or architectures, including droplet-like streamlined contour, large hollow cavity, rough and porous surface with negative potential, and monodisperse size distribution, can be maintained perfectly in a large scale by simply ultrasonically treating *G. lucidum* spores with absolute ethanol. The proper modification of these sculptured architectures provides a cost-effective and scalable approach to produce hybrid structures with high surface areas and absorption abilities. In addition, the use of porous micrometer spore as a carrier of magnetic nanoparticles and fluorescent probes not only makes the magnetic actuation of the spore-based hybrids easy to observe and track under a common optical or fluorescence microscope but also expands the range of propulsion studies of a kind of peculiar structures.

In this study, we develop highly efficient fluorescent magnetic spore–based (spore@Fe_3O_4@CDs) microrobots (FMSMs) for detecting toxins secreted by *C. diff* bacteria (Fig. 1). These microrobots were synthesized rapidly and inexpensively by a stepwise encapsulation and functionalization of the porous natural spores. The resultant FMSMs not only inherit the droplet-like morphology and porous structure well but also display higher specific surface area and excellent functionalities. The incorporation of superior magnetic Fe_3O_4 nanoparticles makes the magnetic actuation of droplet-like microstructure and even similar counterparts feasible in different media, showing continuous and efficient propulsion trajectories. Such a continuous and efficient movement greatly increases the diffusion and mass transport of the detected substance, thus facilitating higher detecting ability than static counterparts. Coupling with functionalized carbon dots (CDs), FMSMs can be tracked in real time through fluorescence emission. The fluorescence change could be observed to detect the presence of *C. diff* toxins within tens of minutes in the bacteria culture medium and even in clinical stool specimens. This suggests that FMSMs show rapid response, high selectivity, and good sensitivity for *C. diff* toxin detection. Such a new active FMSM-based detection platform holds great promise in the rapid detection of bacterial toxins in a broad range of biomedical and biodefense scenarios.

RESULTS

Fabrication and potential application of FMSMs

The preparation of FMSMs involves the combination of facile chemical deposition and subsequent encapsulation and functionalization techniques, as shown in Fig. 1. First, the pretreated *G. lucidum*

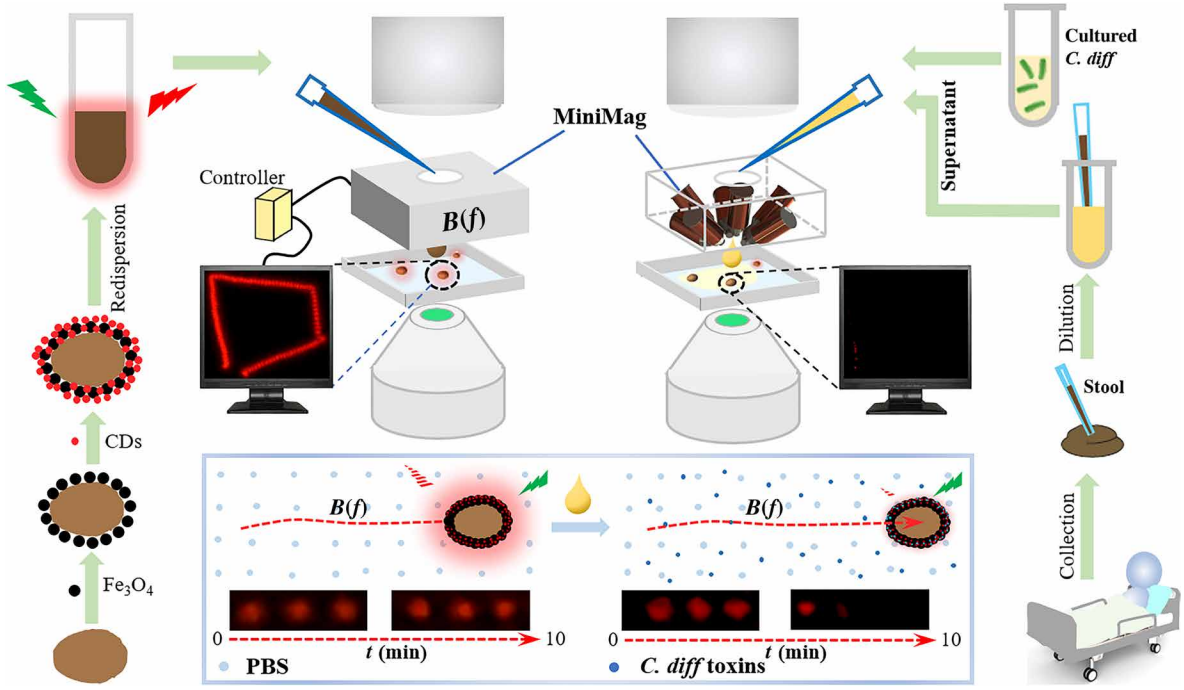

Fig. 1. Schematic illustration of the preparation and potential application of FMSMs. The obtained FMSMs can perform controlled locomotion in predefined tracks to detect the toxins in the supernatant from cultured bacteria and even in a redilution of patients' stool by observing the fluorescence change when being driven continuously in a rotating magnetic field.

spores were encapsulated by a layer of magnetic Fe_3O_4 nanoparticles after chemical bath deposition for 2 hours under a sealed ammonia atmosphere. This step would endow FMSMs with continuous remote magnetic propulsion to produce long-lasting locomotion in various fluids for "on-the-move" reactions. Second, magnetic spores were functionalized with 3-mercaptopropionic acid (MPA) in ethanol at room temperature and conjugated with CDs via carbodiimide chemistry. This functionalization not only makes the mobile FMSM tracking available but also offers a novel capability of targeting *C. diff* toxins and further generating fluorescence quenching for biosensing. The final FMSMs have peculiar morphology, good magnetic property, excellent red fluorescence, and selective targeting ability. We envisage that FMSMs can rapidly detect the *C. diff* toxins in practical samples when used for real-time tracking of their fluorescence changes in a rotating magnetic field equipped with a fluorescence microscope (Fig. 1).

Characterization of FMSMs

As shown in Fig. 2A, evenly distributed intact spores show a droplet-like morphology with an average dimension of approximately 6 to 9 μm. The zoomed-in image in the inset reveals that their surfaces are rough and wrinkled, on which some pores with diameters of 100 to 400 nm are distributed. Moreover, the spore shows a hollow structure and a double-layer wall with a gap of 0.5 to 1.0 μm (fig. S1). The porous and rough surface, together with the surface negative charge demonstrated by the zeta potential (Fig. 2F), would facilitate the absorption of metal ions for further deposition and encapsulation of metal oxides. Magnetic spores are prepared by reaction with ferrous ions under a sealed ammonia atmosphere. A layer of iron oxide nanoparticles is coated onto the original *G. lucidum* spores (Fig. 2B), endowing the spore with the capability of magnetic actuation (magnetization curves in fig. S2) and increasing the surface roughness (table S1). The droplet-like morphology seems to be maintained well in the as-obtained spore hybrids, as shown in Fig. 2B inset and fig. S1B. This encapsulation not only creates the desired propulsion for directional motion without damaging the intricate structure of the original spores but also increases the number of active sites (specific surface area, 10.63 m^2/g; table S1). After further conjugation with CDs via carbodiimide chemistry, the obtained FMSMs still maintain a highly uniform size distribution with an average diameter of approximately 6 to 9 μm and maintain the intact microstructure, rough surface, and hollow interior cavity (Fig. 2C and fig. S1C). The retained pores, together with the assembled nanoparticles on the surface, increase the specific surface area, thus providing more active sites for absorption and reaction, as supported by the isothermal nitrogen adsorption and desorption results (table S1). In comparison to magnetic spores (10.63 m^2/g) and original spores (6.74 m^2/g), FMSMs show increasing Brunauer-Emmett-Teller surface areas of 12.96 m^2/g with a large pore size (>73.2 nm), also superior to the as-reported spherical Janus micromotors (0.0884 to 1.36 m^2/g) and porous hollow helical microswimmers (0.96 to 2.6 m^2/g) (*12*, *22*, *23*). These results indicate that the introduction of magnetic nanoparticles and CDs facilitates the tuning of the surface area of the final FMSMs, thus allowing toxin molecules to readily and freely diffuse in between for subsequent fluorescence quenching. Last, magnetization and good fluorescence emission are enabled in the spore-based microrobots,

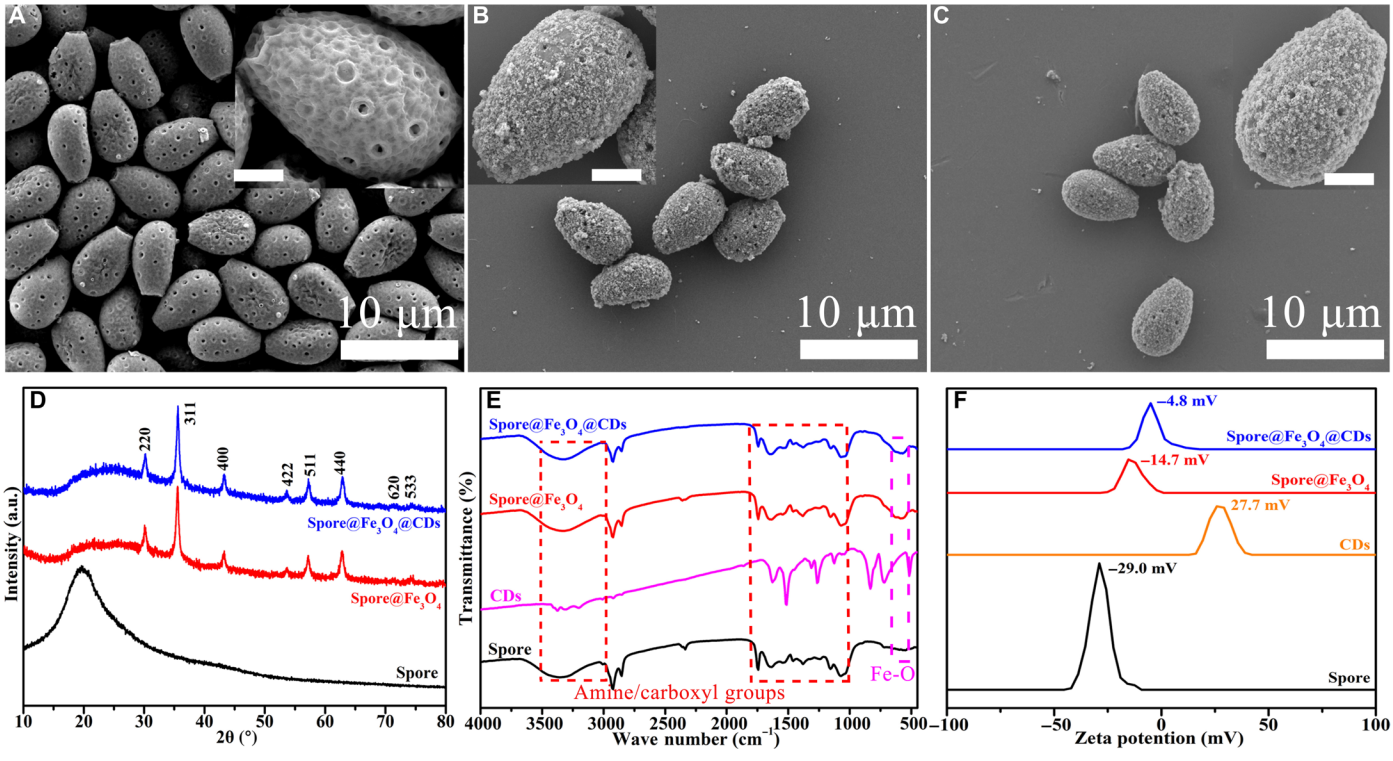

Fig. 2. Structures and compositions of the prepared samples. (**A**) Scanning electron microscopy (SEM) images of the original spores at different magnifications. (**B**) Low- and high-magnification SEM images of spore@Fe_3O_4 hybrids. (**C**) SEM images of hybrid spore@Fe_3O_4@CDs microrobots. Scale bars, 2 μm. XRD patterns (**D**), FTIR spectra (**E**), and zeta potential (**F**) of the original spores and their hybrids. a.u., arbitrary units.

as demonstrated by high magnetization saturation strength in fig. S2, the presence of a magnetic Fe_3O_4 phase (JCPDS card no. 75-1069) in the x-ray diffraction (XRD) patterns (Fig. 2D), and the red fluorescence emission and specific absorption peaks in the fluorescence and ultraviolet-visible (UV-vis) spectra (fig. S3). Moreover, the Fourier transform infrared (FTIR) spectra in Fig. 2E indicate that FMSMs inherit abundant surface functional groups (especially amine and carboxyl groups) from the individual components, and these spectra are similar to the spectra of oligosaccharides in the reported publications (*24*, *25*). These similarities might originate from the formation of oligosaccharides and the related derivative groups on the surface of the CDs during the low-temperature hydrothermal process (*26*, *27*). These functional substances are beneficial for detecting certain amino acid residues due to their specific targeting ability. The above results indicate that biological spores can be coated and functionalized as mobile biohybrid microrobots through rational hybrid design with biocompatible oxides.

Propulsion performance of FMSMs

To date, although the motion of microrobots propelled by various means (e.g., chemical fuel, electric, magnetic, light, and ultrasonic fields) has been studied widely for potential chemo/biosensing applications (*7*, *28*), most of the microrobots were fuel driven and propelled in aqueous solution with some additives, such as H_2O_2, acid, and SDS, which may change the intrinsic nature of the sensing environment. Magnetic actuation is being used especially in biomedical applications because of the remote propulsion and precise motion control, biocompatible raw materials, and harmlessness even with a high-strength magnetic field. In this regard, the rotating magnetic field is provided by a magnetic field generating system (MiniMag MFG-100, MagnebotiX) to first study the magnetic actuation of FMSMs with a novel droplet-like morphology distinct from common helical, spherical, and 1D structures. When a magnetic field is applied in different directions, FMSMs show a consistent and easy magnetization direction along their long axis (fig. S4); the measurement of this magnetization facilitates the establishment of an analysis model of the magnetic actuation. As shown in Fig. 3A, the magnetic actuation of the FMSM shows three motion modes, i.e., spinning, rotation-translation, and tumbling, as the different parameters of the magnetic field are set. When the pitch angle (γ) is 0°, the FMSM almost spins around its center of gravity. When $0° < \gamma < 90°$, the FMSM begins to rotate and translate under the guidance of the direction angle (α), while the FMSM tumbles along the direction of magnetization at $\gamma = 90°$. Because of the magnetization direction along its long axis demonstrated above, the motion of the FMSMs resembles that of a magnetic slender body in a rotating field, such as ellipsoid (*29*) or 1D micro/nanostructure with a magnetization direction along its long axis (*30*, *31*), which enables the FMSMs to locomote in various fluids and ensures efficient detection. These motion modes are further demonstrated by the superimposed snapshots within 7 s in Fig. 3B (taken from movie S1), which indicates that the droplet-like FMSMs can be actuated with control using different magnetic parameters. This lasting and efficient locomotion performance is indispensable for microrobots swimming in a fluid, especially in real body fluid, for further practical application. The 5-second tracking of the FMSMs in fig. S5 (corresponding to movie S2) shows the excellent capabilities for controlled locomotion in deionized water (DIW), phosphate-buffered saline (PBS), Dulbecco's modified Eagle's medium (DMEM), fetal bovine serum (FBS), stomach mucus, and intestinal mucus. Although the viscosity of each medium has a certain effect on the propulsion, FMSMs are capable of performing the locomotion driven by a rotating magnetic field (constant field strength, 10 mT; frequency, 4 Hz). The comparison of the speed of FMSMs measured in different media under different parameters is given in Fig. 3 (C and D). The motion speeds in DIW, PBS, and DMEM gradually increase with enhanced frequency, while the speeds in FBS, interstitial mucus, and mucus first increase then decrease with frequency due to the step-out frequency effect (Fig. 3C) (*32*). Moreover, the difference in speeds is small at lower frequency, from 1.4 to 9.3 μm/s at frequencies below 5 Hz. Figure 3D shows the tendency for speed changes with increased pitch angle. The highest speed can be achieved when the pitch angle is 90° due to the tumbling motion, which is further demonstrated in the inset of the different motion modes in Fig. 3A. Consequently, the magnetically propelled optimal parameters for FMSMs in different media can be determined for practical applications. Despite the lower translational speed (<8.3 μm/s), FMSMs still show motion ability in the viscous mucus collected from a pig's stomach and guts, which could be attributed to their streamline droplet-like morphology, high magnetization strength (about 35.8 electromagnetic unit/g), and the resultant magnetic torques for tumbling motion. Unlike the corkscrew-like motion of helical microrobots (*33*), the tumbling motion, resembling that of 1D micro/nanostructures, allows the magnetized FMSMs to roll along the long axis near a surface at a large pace, thus enabling locomotion in highly viscous biofluids while avoiding a complicated 3D shape design. In addition, the long-term tracking trajectory (99-s tracking from movie S2) illustrates the movement of the FMSM in intestinal mucus, displaying the long-term efficient magnetic propulsion without external perturbation. These results indicate that FMSMs exhibit excellent and stable swimming behavior in different media, ranging from aqueous solution to saline solution and even gastrointestinal tract mucus for visual tracking under a microscope.

Fluorescence property of the FMSM

Once the CDs with fluorescence were conjugated onto the magnetic spores, we observed red fluorescent emission on the final FMSMs with green light excitation (filter, 537 to 552 nm) on an inverted fluorescence microscope (fig. S6), further supported by fluorescence spectra in fig. S3. Figure 3E shows the fluorescence trajectories of FMSMs in DIW, PBS, DMEM, mucus, and intestinal mucus (taken from movie S3). The bright red emission of the FMSM barely fades during the motion, prolonging the observation time and the change of media, indicating good dynamic fluorescence stability. These results indicate that FMSMs inherently show good red fluorescence emission while undergoing locomotion in different media. Such a fluorescence feature might be better for real-time tracking in a biological environment than short-wavelength excitation (generally, ultraviolet light) fluorescence used in H_2O_2-powered microrobots in view of the interference of autofluorescence of biomolecules induced by short-wavelength excitation (*10*, *11*). As illustrated in Fig. 3E, the external media, even real biological samples (mucus), have almost no obvious effects on the fluorescence. Besides, these FMSMs can achieve a more precisely controllable fluorescence motion with automatic and continuous operation along a predefined path, such as the O-, ∞-, and Chinese University (CU)–like trajectories in Fig. 3F (taken from movie S4). This result further extends their multifunctionality and makes them perform well in precise navigation tasks in complicated environments and traffic scenarios.

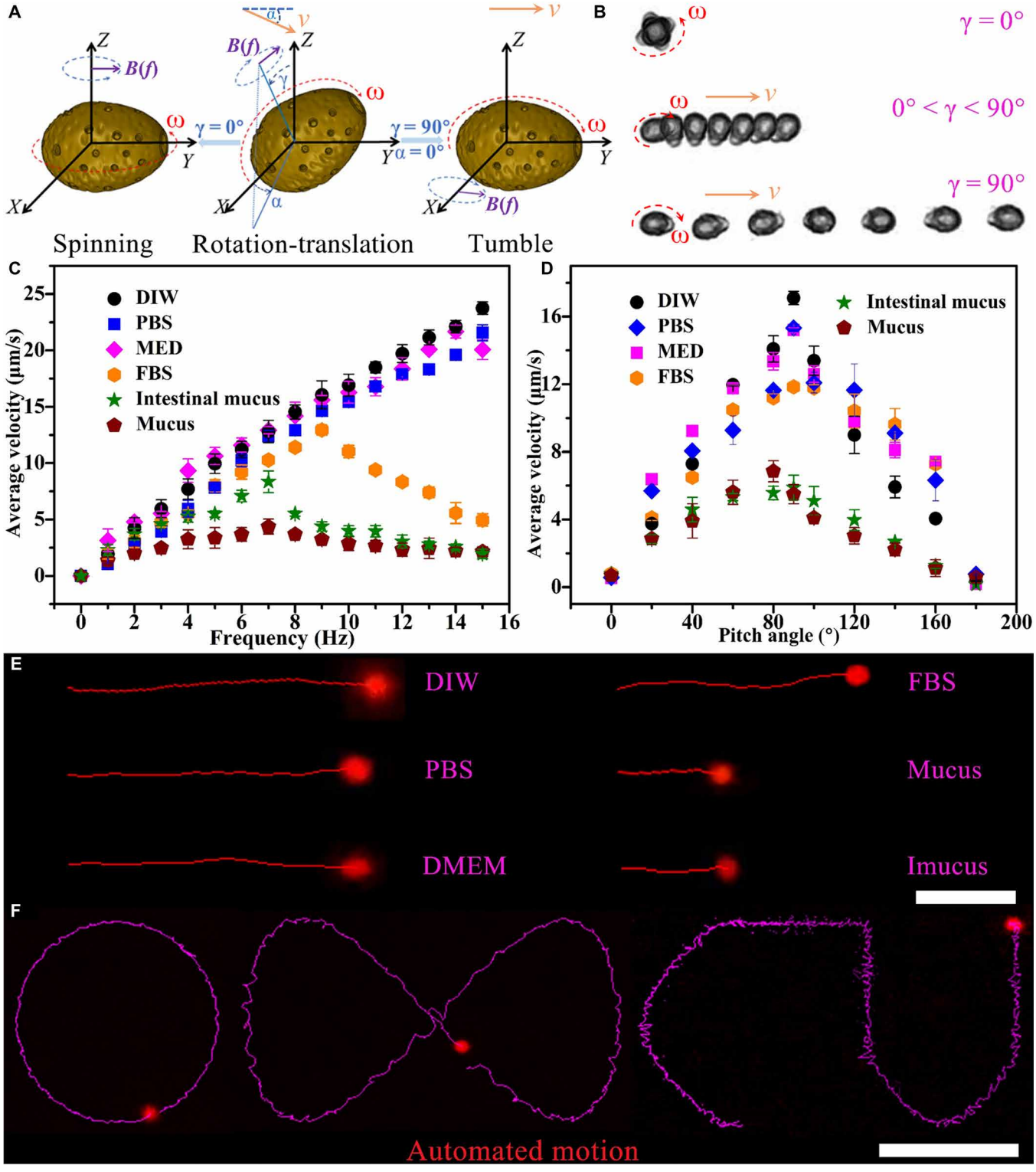

Fig. 3. Swimming and fluorescence performance of FMSMs. (**A**) Schematic illustration of the magnetic actuation for an FMSM, wherein *B* represents the strength of the rotating magnetic field, *f* indicates the input frequency of the magnetic field, *v* represents the translational velocity, ω denotes the rotation velocity, γ denotes the tilt angle between the rotation axis, and α denotes the direction angle. (**B**) Superimposed snapshots of the controlled locomotion of an FMSM within 7 s with different motion modes in a rotating magnetic field (10 mT and 4 Hz, taken from movie S1). (**C**) Speed-frequency relationship at 10 mT with a pitch angle of 40°. (**D**) Speed-pitch angle relationship at 10 mT with a frequency of 4 Hz. (**E**) Fluorescence motion trajectories of the FMSM in DIW, PBS, DMEM, FBS, mucus, and intestinal mucus (Imucus) in a rotating magnetic field within 6 s (10 mT and 4 Hz). Scale bar, 30 μm (taken from movie S3). (**F**) Visual fluorescence trajectories of the autonomous navigation of the FMSM in DIW according to the preset O-, ∞-, and CU-like paths (taken from movie S4). Scale bar, 100 μm.

Detection ability of FMSMs for *C. diff* toxins

We first tested the sensing ability of these FMSMs for *C. diff* toxins in biological samples to demonstrate their practical effectiveness. To ensure good observation and remove background noise from media, we selected the FMSM with bright fluorescence to evaluate fluorescence decay. We measured multiple bright FMSMs (more than six samples) and then took the average intensity. Figure 4 shows the time-dependent fluorescence response of magnetically actuated FMSMs in the bacterial supernatant. The FMSM magnetically navigated for 10 min in the supernatant containing 0.1*C* (here, *C* = 37.60 ng/ml) *C. diff* toxins shows instant fluorescence quenching, while that magnetically navigated in the *Fusobacterium nucleatum* supernatant displays no obvious fluorescence quenching. While the FMSM is magnetically propelled in PBS and brain heart infusion (BHI) medium, no obvious fluorescence fading is observed, even if traveling for 10 min (Fig. 4 and fig. S7). In the control experiment, the static FMSM hardly shows any obvious fluorescence quenching within 10 min in the same supernatant containing 0.1*C C. diff* toxins. This finding not only illustrates the negligible interference effect of other solutes in tested samples but also demonstrates that the active motion has higher detecting efficiency than passive operation due to the accelerated on-the-fly reactions and enhanced fluid mixing (*34*, *35*). The enhanced fluid intermixture in the presence of FMSMs could be further characterized by analyzing the mean squared displacement (MSD) of a passive microtracer [3-μm polystyrene (PS) beads]. We performed experiments by adding 1 ml of aqueous solutions containing 5 μl of the passive microtracer (0.05 mg/ml) and 5 μl of FMSMs (0.05 mg/ml) to a glass tank. The continuous movement of the FMSMs generates a flow field that causes displacement of the passive microtracers (fig. S8, B and C), as compared with the negligible displacement of PS beads undergoing Brownian motion. The resultant MSD plots at a fixed time interval in fig. S8A indicate a marked increase in the presence of active magnetic microrobots compared with that for passive Brownian motion. These results further support the fact that active motion can promote the interaction efficiency between FMSMs and tested samples due to enhanced transport and diffusion of tested samples. We also studied the effect of different toxin concentrations on the detection efficiency. It was found that fluorescence quenching appears rapidly as the toxin concentration increases, as shown in Fig. 4A. The initial extent of fluorescence quenching of the FMSM is directly related to the toxin concentration and decays exponentially with increasing concentration (Fig. 4B). The change curve can be fitted to the equation $F/F_0 = 1.02\exp(C_{toxin}/2.72) + 0.061$, with a correlation coefficient of 0.992 (F and F_0 are the fluorescence intensities of FMSMs before and after the addition of the tested samples, as calculated from the optical density by ImageJ software). There is a good linear relationship between the fluorescence intensity (F/F_0) and the natural logarithm of the toxin concentration ($\ln C_{toxin}$) within the range of 0.38 to 17.80 ng/ml (Fig. 4B, inset). The limit of detection (LOD) is estimated to be 2.13 ng/ml based on the formula LOD = (3SD)/k, where SD is the standard deviation of the corrected blank signal of FMSMs (n = 5) and k is the slope of the calibration curve. The selectivity of such a detection ability was further tested in the presence of an excess concentration (10 mg/ml) of aspartic acid, arginine, glutamic, and lysine as well as the same stock solution of *F. nucleatum* bacteria supernatant and BHI medium (fig. S9) to confirm the targeting ability toward *C. diff* toxins. The static and dynamic results showcase that single amino acid solution and *F. nucleatum* toxin have a negligible effect on the fluorescence intensity of the mobile FMSMs. This selectivity occurs possibly because the oligosaccharide and related groups on FMSMs, which are formed on the surface of the loaded CDs during the hydrothermal process, have a high affinity for amino acid residues (repetitive oligopeptides) on the *C. diff* toxins (*36*–*37*). It is supported by the fact that passive CDs show decaying fluorescence when being added in bacterial supernatant. Moreover, previous reports have demonstrated that *C. diff* toxins can bind carbohydrates (e.g., oligosaccharides) on the cells as an initial step in pathogenesis owing to the presence of combined repetitive oligopeptides (CROPs) in the C-terminal receptor binding domains (*38*–*42*). Thus, the selectivity of FMSMs for *C. diff* toxins can be attributed to the interaction between oligosaccharide and related groups and CROPs, which do not exist in the single amino acid and even in the *F. nucleatum* toxin solution. To further verify the selectivity, we used Smart BLAST (provided by the National Center for Biotechnology Information online) to search the matches of the alignment of the CROPs segment. The survey results in fig. S10 show that the CROPs segment and its high matched sequences can only be observed in toxin A/B and cell wall proteins of *Clostridiodes difficile* in the gastrointestinal

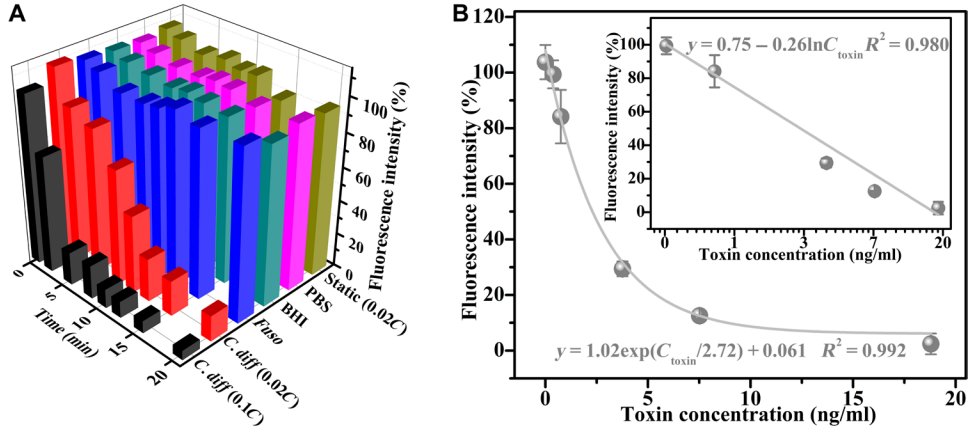

Fig. 4. Fluorescence response of the FMSMs to *C. diff* toxins. (**A**) Changing plot of fluorescence intensity showing the fluorescence quenching in different samples at different times. Here, *C* = 37.60 ng/ml, as determined by enzyme-linked immunosorbent assay (ELISA). *F. nucleatum*, *Fuso*. (**B**) Fluorescence intensity during the FMSMs navigated for 5 min in toxin-contaminated solutions in response to the toxin concentration and the resultant fitting equation. Inset shows the linear relationship between the fluorescence intensity and the natural logarithm of the toxin concentration.

tract and in cholin-binding proteins E/F of bacterium *Streptococcus pneumoniae*, which only exist in the respiratory tract (*43*). These formatting results indicate that other microbial colonies in the gastrointestinal tract have no obvious effect on clinical detection for stool specimens, which greatly supports the effectiveness of specific detection and excludes the possibility of false positives from the interference of other toxins and bacteria in clinical samples. Relying on such a specific interaction (fig. S11), the CDs on FMSMs can conjugate selectively with *C. diff* toxins to form a covalent cross-linked aggregation structure, which results in the well-accepted fluorescence quenching due to surface state changes and fluorescence resonance energy transfer between the CDs and toxin proteins (*12*, *23*, *44*). Eventually, FMSMs have good sensing ability of *C. diff* toxin due to fluorescence quenching induced by specific targeting combination (fig. S11), which would show great potential for the *C. diff* toxin detection in real clinical samples from the gastrointestinal tract.

Practical application in clinical stool samples

The practical use of FMSMs was demonstrated by the ability to detect the toxins in the treated supernatant of clinical stool samples commonly used for ELISA. Considering the controllability of magnetic actuation motion in aqueous solution and practical clinical fluids, we first studied the effect of the motion parameters (speed) and motion modes of FMSMs on their fluorescence quenching. The FMSM moving at high speed showed faster fluorescence quenching than the slowly moving FMSM and the spinning FMSM in the clinical stool supernatant due to the accelerated intermixing and rapid absorption, as shown in fig. S12. Consequently, we still performed the detection of the toxins by manipulating FMSMs in tumbling motion mode to achieve high speed. Figure 5 (A and B) gives the change plots of the fluorescence quenching of static and mobile single FMSMs navigated for different times in various stool samples. The fluorescence intensity of the mobile FMSM (gray column) almost remains stable in the normal stool samples even if the FMSM is navigated at any time at various concentrations of toxins. The static FMSM (cyan column) that remains for 10 min or in 0.1*C* (*C* = 8.66 ng/ml determined from ELISA) infectious stool samples displayed unobvious fluorescence quenching until at higher concentration (>0.5*C*) or for a longer time (>25 min). However, the mobile FMSM showed remarkable fluorescence quenching with the toxins contained in infectious stool at 10 min of navigating time (Fig. 5A) or with the navigating time prolonging at 0.1*C* (Fig. 5B). The extent of fluorescence quenching of FMSMs was still directly proportional to the toxin concentration whether in static or moving status. The corresponding correlations (fig. S13) obey the linear fitting equation $F/F_0 = 1 - 0.019C_{toxin}$ (static) and $F/F_0 = 1 - 0.20C_{toxin}$ (moving), which conform to the Stern-Volmer equation (*23*). The LOD of FMSMs is estimated to be 1.73 ng/ml for motile FMSMs based on the formula (3SD)/*k* (*n* = 5), which is lower than that of H_2O_2-powered microrobots (4 to 7 ng/ml) for other toxins due to fewer side reactions (*10*, *12*, *23*). These results suggest that mobile FMSMs can also effectively detect the toxin in infectious stool samples through sensitive fluorescence quenching. The fluorescence time-lapse images in Fig. 5C (taken from movie S5) further show the detection ability in infectious clinical stool samples where the real biological components did not interfere with the developed assay. Compared with the mobile FMSM in the normal stool supernatant or the static FMSM, the mobile FMSM showed an obvious fluorescence decay in the supernatant of *C. diff*–infectious stool samples with increasing time. In addition, the mobile FMSMs maintained good swimming ability (Fig. 5D) and stable speed (Fig. 5E) even after long-term motion in the stool supernatant at various concentrations, suggesting good anticontamination ability and efficient motion in the tested fluid. Thus, the fluorescence changes can also be reflected by long-term and real-time tracking with continuous manual operation, as shown in Fig. 5F. This characteristic will enable autonomous detection of toxins feasible via an FMSM-based platform in the future, whose potential automated methodology is illustrated in the process flowchart in fig. S14.

DISCUSSION

In conclusion, we have demonstrated the FMSMs and their related sensing application, which are developed by the direct deposition of magnetic nanoparticles and the subsequent encapsulation of sensing probes on the porous natural spores. The FMSMs obtained from these functional micro/nanomaterials show a low-cost, facile, and batch fabrication, superior to the prevalent expensive antibody probes used in ELISA. These mobile microrobots are capable of performing remote sensing of *C. diff* toxins and would be further applied to fast screening of *C. diff* infection based on available fluorescence microscopy and a magnetic actuation system. The presence of *C. diff* toxins can be directly evaluated by observing the fluorescence change of FMSMs in real time. In comparison to their static sensing counterparts dependent on common diffusion, FMSMs exhibit enhanced detection ability by continuous movement due to a great increase in the mass transport of detected substances (i.e., toxins) and the occurrence of the on-the-fly reaction. To our knowledge, conventional ELISA has been used routinely in clinical diagnostics for the detection of *C. diff* toxins due to its reliability, sensitivity, and specificity. Nevertheless, it is still a big challenge to integrate low cost, high sensitivity, and shorter operation time into the use of ELISA simultaneously. Benefiting from an on-the-move reaction based on continuous motion, active detection using FMSMs might provide a promising solution to these issues accordingly. The screening of toxins using FMSMs in bacterial medium and clinical stool supernatants has been demonstrated and shows high selectivity and good sensitivity. The LOD of the FMSMs (1.73 ng/ml) is comparable to that of some of the highest-performing ELISA (ranging from 0.8 to 2.5 ng/ml) in stool samples (*45*). The analysis time is at least eight times shorter than that of conventional ELISA. Given that *C. diff* toxins degrade readily at room temperature and are denatured by other factors, shorter analysis time and good detection ability make FMSMs suitable and a candidate for sensing *C. diff* toxins in clinical stool specimens. Through the introduction of different targeted functional groups, such an FMSM-based detection platform also holds great promise for the detection of a broad range of chemical or biological toxins. The two-step encapsulation strategy can also be extended to other natural spores for the fabrication of hybrid micro/nanorobots.

As suggested by previous publications, the application of micro/nanorobots for detecting pathogenic bacteria and toxins that pose threats to our body is still at an early stage. At present, some proof-of-concept studies have been demonstrated in the laboratory, but the further practical use is still limited by the complexity of detection environments. It is thus necessary to further improve and evaluate FMSMs before their potential application. With these biohybrid microrobots, we have achieved the detection of *C. diff* toxins in pretreated clinical stool samples, similar to those used in ELISA. Consequently, the capability of detecting bacterial toxins and even bacteria of these

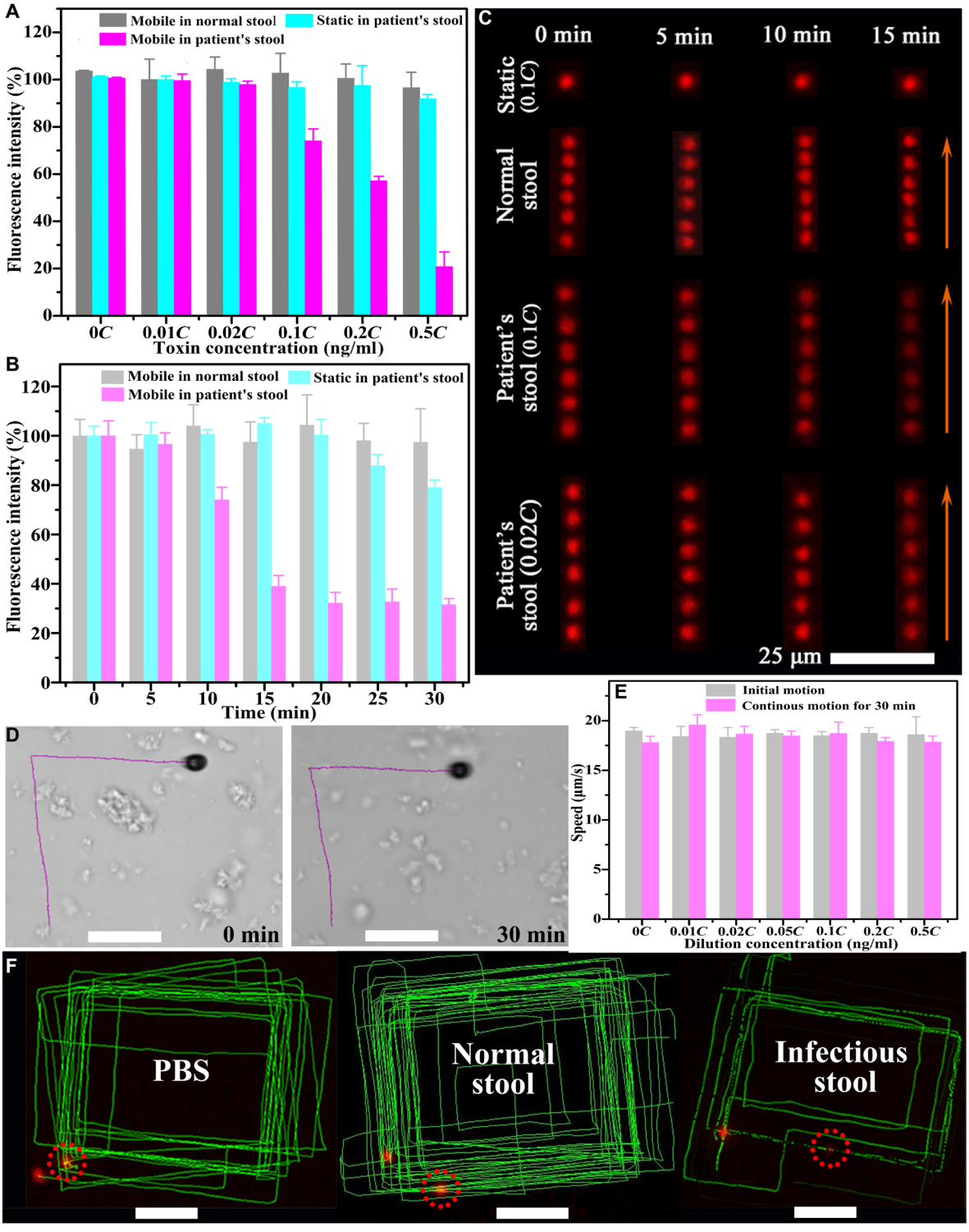

Fig. 5. Fluorescence detection in stool supernatant using the FMSMs. The changing trend of the fluorescence intensity of static and mobile FMSMs (**A**) navigated for 10 min in different stool samples and (**B**) traveling for different times in 0.1*C* (*C* = 8.66 ng/ml) stool samples. (**C**) Fluorescence time-lapse images of static and mobile FMSMs with a time interval of 1 s at different times in different clinical stool supernatants (taken from movie S5). (**D**) Tracking for 8 s showing the propulsion of FMSMs in the infectious stool supernatant at the beginning and after 30 min. (**E**) Speed comparison of the FMSMs navigated for 0 and 30 min in the clinical infectious stool supernatant. (**F**) Tracking fluorescence trajectories of the FMSMs locomoting for approximately 18 min in different samples. Scale bars, 30 μm.

biohybrid microrobots offers considerable interest for active (bio) sensing applications. These biohybrid microrobots that integrate with multifunctionality are expected to offer chances and inspire novel ideas for rapidly emerging microrobotic applications.

MATERIALS AND METHODS

Materials and chemicals

G. lucidum spores were purchased from a cultured farm in Changbai Mountain, Jilin Province, China. Ferrous sulfate heptahydrate ($FeSO_4{\cdot}7H_2O$), ammonia ($NH_3{\cdot}H_2O$), glucose, and *p*-phenylenediamine were purchased from Aladdin Chemistry Co. Ltd. (Shanghai, China) and used as received without further purification. PBS, DMEM, BHI culture medium, and FBS were purchased from Thermo Fisher Scientific Incorporation. MPA, 1-ethyl-3-(3-dimethylaminopropyl)carbodiimide (EDC), *N*-hydroxysuccinimide (NHS), lysine, glutamic, arginine, and aspartic acid were purchased from Sigma-Aldrich. Mucus was scratched from fresh pig stomach, and guts were purchased from a local market. *F. nucleatum* and *C. diff* culture media were provided by W.K.K.W. (Department of Anaesthesia and Intensive Care, Faculty of Medicine, Chinese University of Hong Kong). Clinical stool samples from healthy volunteers and *C. diff*–positive patients were provided by S.H.W. (Department of Medicine and Therapeutics, Faculty of Medicine, Chinese University of Hong Kong). DIW with a resistance of 18.2 megohm (Smart2Pure 12, Thermo Fisher Scientific) was used throughout the experiments.

Synthesis of magnetic spore@Fe_3O_4

G. lucidum spores were first pretreated to remove the impurities on the exine and internal core substances. Five grams of spores was dispersed into 200 ml of absolute ethanol under ultrasonic treatment for 30 min. Then, they were redispersed into 200 ml of DIW for 10 min of ultrasonication, followed by rinsing with DIW several times and freeze drying. The resultant spores were used to prepare magnetic spores through a facile chemical bath deposition of Fe_3O_4 nanoparticles on their surface. In a typical synthesis, 200 mg of spores was dispersed into 60 ml of DIW with the assistance of ultrasonication and stirred for 5 min to form the brown suspension. Then, 100 mg of $FeSO_4$ was added into the above suspension and stirred for 20 min to ensure complete absorption of spore surface toward Fe^{2+}. Afterward, 20 ml of ammonia (25 to 27 weight %) was added dropwise within 10 min, sealed, and further stirred for 2 hours. The brownish black precipitation was collected with a magnet, washed with ethanol and DIW several times, and freeze dried.

To conjugate with fluorescent CDs, surface modification of magnetic spore with MPA was necessary. The brownish black samples were dispersed into 200 ml of ethanol and stirred for 10 min to form a homogenous suspension, followed by the addition of 0.2 mmol of MPA. The mixed suspension was stirred for 10 min and stayed at room temperature for 24 hours. After being collected with a magnet, the carboxyl functionalized magnetic spores were washed with ethanol three times to remove residual MPA and then freeze dried for the next preparation.

Functionalized fluorescent carbon dots (CDs) were obtained by facile hydrothermal treatment of small molecules. Aspartic acid (0.16 g), glucose (0.16 g), and *p*-phenylenediamine (0.16 g) were dissolved in 40 ml of water and transferred into a Teflon-lined stainless steel autoclave. After being heated at 180°C for 10 hours and then cooled down to room temperature, the obtained solution was separated by vacuum filtration (0.22-μm nitrocellulose filters), followed by dialysis with a dialysis membrane (molecular weight cutoff, 3500) for 24 hours. The transparent light brown solution was stored at 4°C, and a small amount (about 2 ml) was taken to determine its concentration after heat evaporation (about 5.8 mg/ml).

Synthesis of fluorescent magnetic spore@Fe_3O_4@CDs microrobots

Fluorescent spore@Fe_3O_4@CDs microrobots were obtained using EDC/NHS coupling chemistry. Fifty milligrams of functionalized magnetic spores was dispersed into 60 ml of DIW under ultrasonication for 5 min. Then, 0.5 mmol of EDC and 0.5 mmol of NHS were added and stirred for 2 hours to activate the carboxyl groups on the samples. After adding 20 ml of the as-obtained CDs, the mixed suspension was allowed to react at room temperature for 24 hours under gentle stirring. Last, the samples were collected by a magnet, washed with ethanol and DIW several times, and freeze dried for further use.

Instrumentation and characterization

The microstructures and sizes of the samples were taken by a JSM-7800F field emission scanning electron microscope (JEOL-7800F, Japan). Optical images were captured by a Nikon Eclipse Ti inverted fluorescence microscope (Nikon, Japan) equipped with a Photometrics Prime sCMOS (scientific complementary metal-oxide-semiconductor) camera (Photometrics Company, USA). Fluorescence imaging was carried out on the above inverted fluorescence microscope under green light excitation (filter, 537 to 552 nm). XRD analysis was performed using a SmartLab diffractometer (Rigaku, Japan) with Cu Kα radiation of 1.54059-Å wavelength between 5° and 80°. The surface composition was recorded using an FTIR (Thermo Nicolet Nexus 670, USA) spectrometer with KBr pellets. UV-vis spectrum was taken on a U2910 double beam UV-vis spectrophotometer (Hitachi, Japan). Fluorescence spectra were measured on a Hitachi F-7000 spectrophotometer (Hitachi, Japan) equipped with a 1-cm quartz cuvette at room temperature. The excitation and emission slit widths were set at 10 and 10 nm, respectively. Zeta potentials were conducted on a Zetasizer Nano ZS instrument (Malvern, UK).

Magnetic properties and corresponding actuation testing

Magnetic performance of the fluorescent magnetic microrobot was obtained using a vibrating sample magnetometer (Physical Property Measurement System Model 6000, Quantum Design, USA) at room temperature. Motion control and magnetotaxis experiments were conducted and observed on an inverted microscopy equipped with a magnetic field generating system (MiniMag MFG-100, MagnebotiX, Switzerland). Zero to 5 μl of microrobot suspension (0.05 mg/ml) was dispersed into 0.1 to 1 ml of different media in a glass-bottom tank. Optical and fluorescence videos were acquired in different media after magnetically propelling microrobots at different time intervals. Selectivity experiments were performed in a similar fashion. Videos and images were processed with ImageJ software developed by the National Institutes of Health. The fluorescence intensity of the FMSMs in the images and videos was measured and calculated using the ImageJ software. Initially, the integrated density, actual area, and background fluorescence noise of individual FMSM can be measured directly with the ImageJ software from the captured fluorescence images. Then, the optical density of the FMSM can be obtained through dividing the integrated density by its area and then deducting the background fluorescence readings per area. Last, the fluorescence intensity of the

FMSM can be calculated through dividing the actual calculated optical density in the tested samples by initial optical density before starting the sensing process.

C. diff toxin detection

The supernatant of *C. diff* culture media was used without further treatment, while the solid stool specimens (about 2 g) were cut, redispersed in 2 ml of PBS, and then made to supernatant for use. The initial concentration was determined by standard ELISA using the *C. diff* toxins A and B ELISA Kit (TGC-E002-1, tgcBIOMICS GmbH, Germany). The stock solution was diluted into different concentrations (0.01*C* to 0.5*C*, *C* is the initial concentration determined by ELISA) before the sensing experiments and stored at −20°C. Control experiments were also performed in a similar fashion. The microrobot suspension was added into the above diluted solution, and then, the fluorescence changes of the fluorescent magnetic microrobots navigated for different times in the diluted solution were observed and recorded through an inverted fluorescence microscope. The presence of *C. diff* toxins would quench the fluorescence of the fluorescent magnetic microrobots with the microrobots moving within a certain duration. The data were obtained through averaging the results of three sets of the same bacteria media and the clinical samples from healthy volunteers and *C. diff*–positive patients.

SUPPLEMENTARY MATERIALS

Supplementary material for this article is available at http://advances.sciencemag.org/cgi/content/full/5/1/eaau9650/DC1

Fig. S1. Cross-section SEM images of the prepared samples.
Fig. S2. Magnetization curves of the prepared samples.
Fig. S3. Optical properties of the prepared samples.
Fig. S4. Magnetization direction of multiple FMSMs and single FMSM.
Fig. S5. Motion trajectories of an FMSM in various media over 5-s time frames.
Fig. S6. Optical images of the FMSMs under different illuminations.
Fig. S7. Fluorescence time-lapse images of static and moving FMSMs in bacterial supernatants.
Fig. S8. MSD of the microtracers caused by the motion of the FMSMs.
Fig. S9. Fluorescence responses of the FMSMs toward different substances.
Fig. S10. The survey results of the alignment of CROP segment of *C. diff* toxin B (amino acids 1830 to 2366) using Smart BLAST provided by the National Center for Biotechnology Information online.
Fig. S11. Schematic for the structures of *C. diff* toxins and mechanism of quenching by the CROP segment of *C. diff* toxins to CDs on the FMSMs.
Fig. S12. Fluorescence changes in different motion modes.
Fig. S13. Detection calibration curves of the FMSMs.
Fig. S14. Future automated control detection strategy.
Table S1. Specific surface areas and pore parameters of the samples.
Movie S1. Magnetic actuation of the FMSMs using a rotating magnetic field.
Movie S2. Swimming of the FMSMs in different media.
Movie S3. Fluorescence tracking of the FMSMs in different media.
Movie S4. Automated fluorescence signal–based servoing of the FMSMs in predefined trajectories.
Movie S5. Fluorescence detection using the FMSMs in clinical stool supernatant.

REFERENCES AND NOTES

1. S. S. Magill, J. R. Edwards, W. Bamberg, Z. G. Beldavs, G. Dumyati, M. A. Kainer, R. Lynfield, M. Maloney, L. McAllister-Hollod, J. Nadle, S. M. Ray, D. L. Thompson, L. E. Wilson, S. K. Fridkin, Multistate point-prevalence survey of health care–associated infections. *N. Engl. J. Med.* **370**, 1198–1208 (2014).
2. M. Rupnik, M. H. Wilcox, D. N. Gerding, *Clostridium difficile* infection: New developments in epidemiology and pathogenesis. *Nat. Rev. Microbiol.* **7**, 526–536 (2009).
3. R. N. Pruitt, D. B. Lacy, Toward a structural understanding of *Clostridium difficile* toxins A and B. *Front. Cell. Infect. Microbiol.* **2**, 28 (2012).
4. L. Alcalá, L. Sanchez-Cambronero, M. P. Catalán, M. Sanchez-Somolinos, M. T. Peláez, M. Marín, E. Bouza, Comparison of three commercial methods for rapid detection of *Clostridium difficile* toxins A and B from fecal specimens. *J. Clin. Microbiol.* **46**, 3833–3835 (2008).
5. F. C. Tenover, S. Novak-Weekley, C. W. Woods, L. R. Peterson, T. Davis, P. Schreckenberger, F. C. Fang, A. Dascal, D. N. Gerding, J. H. Nomura, R. V. Goering, T. Akerlund, A. S. Weissfeld, E. J. Baron, E. Wong, E. M. Marlowe, J. Whitmore, D. H. Persing, Impact of strain type on detection of toxigenic *Clostridium difficile*: Comparison of molecular diagnostic and enzyme immunoassay approaches. *J. Clin. Microbiol.* **48**, 3719–3724 (2010).
6. F. Wong, K. K. Dey, A. Sen, Synthetic micro/nanomotors and pumps: Fabrication and applications. *Annu. Rev. Mater. Res.* **46**, 407–432 (2016).
7. A. Chałupniak, E. Morales-Narváez, A. Merkoçi, Micro and nanomotors in diagnostics. *Adv. Drug Deliv. Rev.* **95**, 104–116 (2015).
8. J. Wang, Self-propelled affinity biosensors: Moving the receptor around the sample. *Biosens. Bioelectron.* **76**, 234–242 (2016).
9. B. Esteban-Fernández de Ávila, M. A. Lopez-Ramirez, D. F. Báez, A. Jodra, V. V. Singh, K. Kaufmann, J. Wang, Aptamer-modified graphene-based catalytic micromotors: Off–on fluorescent detection of ricin. *ACS Sens.* **1**, 217–221 (2016).
10. A. Molinero-Fernández, A. Jodra, M. Moreno-Guzmán, M. Á. López, A. Escarpa, Magnetic reduced graphene oxide/nickel/platinum nanoparticles micromotors for mycotoxin analysis. *Chemistry* **24**, 7172–7176 (2018).
11. Á. Molinero-Fernández, M. Moreno-Guzmán, M. Á. López, A. Escarpa, Biosensing strategy for simultaneous and accurate quantitative analysis of mycotoxins in food samples using unmodified graphene micromotors. *Anal. Chem.* **89**, 10850–10857 (2017).
12. M. Pacheco, B. Jurado-Sánchez, A. Escarpa, Sensitive monitoring of enterobacterial contamination of food using self-propelled Janus microsensors. *Anal. Chem.* **90**, 2912–2917 (2018).
13. B. Xu, B. Zhang, L. Wang, G. Huang, Y. Mei, Tubular micro/nanomachines: From the basics to recent advances. *Adv. Funct. Mater.* **28**, 1705872 (2018).
14. P. Yánez-Sedeño, S. Campuzano, J. M. Pingarrón, Janus particles for (bio)sensing. *Appl. Mater. Today* **9**, 276–288 (2017).
15. M. Zarei, M. Zarei, Self-propelled micro/nanomotors for sensing and environmental remediation. *Small* **14**, 1800912 (2018).
16. J. Parmar, D. Vilela, K. Villa, J. Wang, S. Sánchez, Micro- and nanomotors as active environmental microcleaners and sensors. *J. Am. Chem. Soc.* **140**, 9317–9331 (2018).
17. T. Ariizumi, K. Toriyama, Genetic regulation of sporopollenin synthesis and pollen exine development. *Annu. Rev. Plant Biol.* **62**, 437–460 (2011).
18. M. G. Potroz, R. C. Mundargi, J. J. J. Gillissen, E.-L. Tan, S. Meker, J. H. Park, H. Jung, S. Park, D. Cho, S.-I. Bang, N.-J. Cho, Plant-based hollow microcapsules for oral delivery applications: Toward optimized loading and controlled release. *Adv. Funct. Mater.* **27**, 1700270 (2017).
19. R. C. Mundargi, M. G. Potroz, S. Park, H. Shirahama, J. H. Lee, J. Seo, N. J. Cho, Natural sunflower pollen as a drug delivery vehicle. *Small* **12**, 1167–1173 (2016).
20. X. Yan, Q. Zhou, M. Vincent, Y. Deng, J. Yu, J. Xu, T. Xu, T. Tang, L. Bian, Y.-X. J. Wang, K. Kostarelos, L. Zhang, Multifunctional biohybrid magnetite microrobots for imaging-guided therapy. *Sci. Robot.* **2**, eaaq1155 (2017).
21. G.-Z. Yang, J. Bellingham, P. E. Dupont, P. Fischer, L. Floridi, R. Full, N. Jacobstein, V. Kumar, M. McNutt, R. Merrifield, B. J. Nelson, B. Scassellati, M. Taddeo, R. Taylor, M. Veloso, Z. L. Wang, R. Wood, The grand challenges of *Science Robotics*. *Sci. Robot.* **3**, eaar7650 (2018).
22. X.-H. Yan, Q. Zhou, J. Yu, T. Xu, Y. Deng, T. Tang, Q. Feng, L. Bian, Y. Zhang, A. Ferreira, L. Zhang, Magnetite nanostructured porous hollow helical microswimmers for targeted delivery. *Adv. Funct. Mater.* **25**, 5333–5342 (2015).
23. B. Jurado-Sánchez, M. Pacheco, J. Rojo, A. Escarpa, Magnetocatalytic graphene quantum dots Janus micromotors for bacterial endotoxin detection. *Angew. Chem.* **129**, 7061–7065 (2017).
24. A. López-Cruz, C. Barrera, V. L. Calero-DdelC, C. Rinaldi, Water dispersible iron oxide nanoparticles coated with covalently linked chitosan. *J. Mater. Chem.* **19**, 6870–6876 (2009).
25. J. Liu, H. Li, J. Wu, F. Xie, J. Zhang, Z. Wang, Determination of phosphoryl-oligosaccharides obtained from Canna edulis Ker starch. *Starch* **69**, 1500263 (2017).
26. B. Gullón, R. Yáñez, J. L. Alonso, J. C. Parajó, Production of oligosaccharides and sugars from rye straw: A kinetic approach. *Bioresour. Technol.* **101**, 6676–6684 (2010).
27. M. Martínez, R. Yáñez, J. L. Alonsó, J. C. Parajó, Chemical production of pectic oligosaccharides from orange peel wastes. *Ind. Eng. Chem. Res.* **49**, 8470–8476 (2010).
28. K. Kim, J. Guo, Z. Liang, D. Fan, Artificial micro/nanomachines for bioapplications: Biochemical delivery and diagnostic sensing. *Adv. Funct. Mater.* **28**, 1705867 (2018).
29. O. Güell, F. Sagués, P. Tierno, Magnetically driven Janus micro-ellipsoids realized via asymmetric gathering of the magnetic charge. *Adv. Mater.* **23**, 3674–3679 (2011).
30. R. S. M. Rikken, R. J. M. Nolte, J. C. Maan, J. C. M. van Hest, D. A. Wilson, P. C. M. Christianen, Manipulation of micro- and nanostructure motion with magnetic fields. *Soft Matter* **10**, 1295–1308 (2014).
31. L. Zhang, T. Petit, Y. Lu, B. E. Kratochvil, K. E. Peyer, R. Pei, J. Lou, B. J. Nelson, Controlled propulsion and cargo transport of rotating nickel nanowires near a patterned solid surface. *ACS Nano* **4**, 6228–6234 (2010).

32. L. Zhang, J. J. Abbott, L. Dong, K. E. Peyer, B. E. Kratochvil, H. Zhang, C. Bergeles, B. J. Nelson, Characterizing the swimming properties of artificial bacterial flagella. *Nano Lett.* **9**, 3663–3667 (2009).
33. D. Walker, B. T. Käsdorf, H.-H. Jeong, O. Lieleg, P. Fischer, Enzymatically active biomimetic micropropellers for the penetration of mucin gels. *Sci. Adv.* **1**, e1500501 (2015).
34. D. Rojas, B. Jurado-Sánchez, A. Escarpa, "Shoot and sense" Janus micromotors-based strategy for the simultaneous degradation and detection of persistent organic pollutants in food and biological samples. *Anal. Chem.* **88**, 4153–4160 (2016).
35. B. Jurado-Sánchez, A. Escarpa, Milli, micro and nanomotors: Novel analytical tools for real-world applications. *TrAC Trends Anal. Chem.* **84**, 48–59 (2016).
36. A. El-Hawiet, E. N. Kitova, P. I. Kitov, L. Eugenio, K. K. S. Ng, G. L. Mulvey, T. C. Dingle, A. Szpacenko, G. D. Armstrong, J. S. Klassen, Binding of *Clostridium difficile* toxins to human milk oligosaccharides. *Glycobiology* **21**, 1217–1227 (2011).
37. M. Zheng, S. Ruan, S. Liu, T. Sun, D. Qu, H. Zhao, Z. Xie, H. Gao, X. Jing, Z. Sun, Self-targeting fluorescent carbon dots for diagnosis of brain cancer cells. *ACS Nano* **9**, 11455–11461 (2015).
38. A. Greco, J. G. S. Ho, S.-J. Lin, M. M. Palcic, M. Rupnik, K. K.-S. Ng, Carbohydrate recognition by *Clostridium difficile* toxin A. *Nat. Struct. Mol. Biol.* **13**, 460–461 (2006).
39. L. Tao, J. Zhang, P. Meraner, A. Tovaglieri, X. Wu, R. Gerhard, X. Zhang, W. B. Stallcup, J. Miao, X. He, J. G. Hurdle, D. T. Breault, A. L. Brass, M. Dong, Frizzled proteins are colonic epithelial receptors for *C. difficile* toxin B. *Nature* **538**, 350–355 (2016).
40. J. G. S. Ho, A. Greco, M. Rupnik, K. K.-S. Ng, Crystal structure of receptor-binding C-terminal repeats from *Clostridium difficile* toxin A. *Proc. Natl. Acad. Sci. U.S.A.* **102**, 18373–18378 (2005).
41. T. Dingle, S. Wee, G. L. Mulvey, A. Greco, E. N. Kitova, J. Sun, S. Lin, J. S. Klassen, M. M. Palcic, K. K. S. Ng, G. D. Armstrong, Functional properties of the carboxy-terminal host cell-binding domains of the two toxins, TcdA and TcdB, expressed by *Clostridium difficile*. *Glycobiology* **18**, 698–706 (2008).
42. T. Jank, K. Aktories, Structure and mode of action of clostridial glucosylating toxins: The ABCD model. *Trends Microbiol.* **16**, 222–229 (2008).
43. A. Kadioglu, J. N. Weiser, J. C. Paton, P. W. Andrew, The role of *Streptococcus pneumoniae* virulence factors in host respiratory colonization and disease. *Nat. Rev. Microbiol.* **6**, 288–301 (2008).
44. X. Sun, Y. Lei, Fluorescent carbon dots and their sensing applications. *Trends Anal. Chem.* **89**, 163–180 (2017).
45. N. R. Pollock, Ultrasensitive detection and quantification of toxins for optimized diagnosis of *Clostridium difficile* infection. *J. Clin. Microbiol.* **54**, 259–264 (2016).

Acknowledgments: We thank the technical assistance from other members in Prof. Wong's and Wu's lab in Princess of Wales Hospital and S. Wang for the support of SEM inspection. **Funding:** This work was partially supported by the General Research Fund (GRF) with project nos. 14209514, 14203715, and 14218516 from the Research Grants Council (RGC) of Hong Kong SAR, the HKSAR Innovation and Technology Commission (ITC) with ITF project no. ITS/231/15 and ITS/440/17FP, and the Health and Medical Research Fund (HMRF) with project no. 15140132 (W.K.K.W.). **Author contributions:** Y.Z. designed and conducted the experiments, analyzed the results, and wrote the manuscript. W.K.K.W. and Lin Zhang provided the bacterial supernatant, assisted with the detection tests, and contributed to the discussion of the results. L.Y. and C.I.V. supported the automated motion experiments. K.F.C., P.W.Y.C., and J.J.Y.S. contributed to the discussion of experiments and editing of the manuscript. W.K.K.W., T.N.Y.K., N.W.S.L., M.I., and S.H.W. provided the samples and contributed to the discussion of the results. Li Zhang supervised this work, guided the discussion, and edited the manuscript. **Competing interests:** Lin Zhang, Y.Z., L.Y., K.F.C., Li Zhang, and W.K.K.W. are inventors on a nonprovisional patent application related to this work filed by the United States Patent and Trademark Office (no. 16175024, filed 30 October 2018). The authors declare no other competing interests. **Data and materials availability:** All data needed to evaluate the conclusions in the paper are present in the paper and/or the Supplementary Materials. Additional data related to this paper may be requested from the authors.

Submitted 1 August 2018
Accepted 30 November 2018
Published 11 January 2019
10.1126/sciadv.aau9650

Citation: Y. Zhang, L. Zhang, L. Yang, C. I. Vong, K. F. Chan, W. K. K. Wu, T. N. Y. Kwong, N. W. S. Lo, M. Ip, S. H. Wong, J. J. Y. Sung, P. W. Y. Chiu, L. Zhang, Real-time tracking of fluorescent magnetic spore–based microrobots for remote detection of *C. diff* toxins. *Sci. Adv.* **5**, eaau9650 (2019).